

Accepted manuscript

Hu, W., Chen, W., Wang, X., Jiang, Z., Wang, Y., Verma, A. & Teuwen, J. J. (2021). A computational framework for coating fatigue analysis of wind turbine blades due to rain erosion. *Renewable Energy*, 170, 236-250.

Published in: Renewable Energy

DOI: <https://doi.org/10.1016/j.renene.2021.01.094>

AURA: <https://hdl.handle.net/11250/3073477>

Copyright: © 2021 Elsevier

License: CC BY NC ND

Embargo: Available from 22. January 2023.

1 **Computational Framework for Coating Fatigue Analysis of Wind Turbine Blades Due to**
2 **Rain Erosion**

3 **Weifei Hu^{1,2*}, Weiyi Chen^{1,2}, Xiaobo Wang², Zhiyu Jiang³, Yeqing Wang⁴, Amrit Verma⁵,**
4 **Julie Teuwen⁵**

5 ¹ State Key Laboratory of Fluid Power and Mechatronic Systems, Zhejiang University, Hangzhou
6 310027, China

7 ² School of Mechanical Engineering, Zhejiang University, Hangzhou 310027, China

8 ³ Department of Engineering Sciences, University of Agder, N-4898 Grimstad, Norway

9 ⁴ Department of Mechanical and Aerospace Engineering, Syracuse University, Syracuse, NY
10 13244, USA

11 ⁵ Delft University of Technology, Faculty of Aerospace Engineering Delft, Netherlands

12

13 *Corresponding author: Weifei Hu (weifeihu@zju.edu.cn)

14

15 **Abstract**

16 The rain-induced fatigue damage in the wind turbine blade coating has attracted increasing
17 attention owing to repair and maintenance costs. The existing computational models for estimating
18 the coating fatigue life have not well addressed many important issues, such as the realistic rain
19 event simulation, raindrop impact stress calculation, and fatigue analysis considering crack
20 initiation and propagation periods. By including these aspects, the present paper develops an

21 improved computational framework for analyzing the wind turbine blade coating fatigue induced
22 by rain erosion. The paper first presents an extended stochastic rain field simulation model that
23 considers different raindrop shapes (spherical, flat, and spindle), raindrop sizes, impact angles, and
24 impact velocities. The influence of these raindrop characteristics on the impact stress of the blade
25 coating is investigated by a smoothed particle hydrodynamic approach. To address the expensive
26 computational time, a stress interpolation method is proposed to calculate the impact stress of all
27 raindrops in a random rain event. Furthermore, coating fatigue analysis is performed by including
28 the fatigue crack initiation in the erosion incubation period and the fatigue crack propagation in
29 the mass-loss-rate increasing period due to raindrop impact. Finally, the proposed computational
30 framework is verified by comparing the estimated fatigue life with those obtained in literature. The
31 results from the study show that by incorporating the statistics of rainfall data, the proposed
32 framework could be used to calculate the expected fatigue life of the blade coating due to rain
33 erosion.

34 **Keywords:** wind turbine blade, rain erosion, raindrop impact, fatigue analysis, crack propagation,
35 smoothed particle hydrodynamic

36

37 **1 INTRODUCTION**

38 Wind turbine blades (WTBs), especially at tip sections, are frequently exposed to impacts
39 from high-relative-speed objects such as rain, atmospheric particles, hail, and sand during the
40 service life. These impacts may induce erosion damage at the blade leading edge, thereby reducing
41 the aerodynamic performance and power output of wind turbines. In addition, such issues require
42 regular maintenance and repair, causing an increase in the cost of energy. The issue of leading

43 edge erosion (LEE) of WTBs is becoming even more crucial as wind turbines continue to grow in
44 both hub-height and rotor diameter and are associated with large tip speeds.

45 Among the above-stated impacts from relatively high-speed objects, raindrop impact is one
46 of the most important factors that contributes to LEE of WTBs. Traditionally, there are two
47 approaches utilized for analyzing the rain erosion problem, the impact approach (e.g., [1]) or the
48 energetic approach (e.g., [2]). The former approach first calculates the impact pressure using either
49 explicit formulas, e.g., the water-hammer equations [3, 4], or the expensive computational fluid
50 dynamic (CFD) methods (e.g. [5]), then carries out the transient stress analysis by applying the
51 pressure force on the finite element model of a WTB (e.g., [5]). Although it is less computationally
52 intensive to calculate pressure by the explicit water-hammer equations, the following assumptions
53 are made: (1) the impact occurs in one dimension and (2) the impact solid is a perfect rigid body
54 [3], which do not realistically represent raindrop impacts. In addition, it is difficult to take into the
55 account the fluid-solid interaction during raindrop impact by sequentially calculating the impact
56 pressure and the transient stress. The energetic approach attempts to relate the erosion to
57 mechanical properties of the impact body based on the kinetic energy transmitted. Although this
58 approach can potentially avoid simplifications (e.g., the impact effects are independent of each
59 raindrop and the shape of raindrops is a perfect sphere), it is difficult to quantify the total
60 transferred energy from the stochastic rain field to the WTB.

61 A high-fidelity simulation of rain events is essential for accurately predicting the erosion
62 process. However, as rain events are complex natural phenomena, it is challenging to simulate
63 them realistically due to varying raindrop sizes, shapes, and speeds. By integrating the micro-
64 structural properties of rain, i.e., raindrop sizes and spatial distribution, a stochastic rain texture
65 model is developed to generate three-dimensional rain fields by Amirzadeh et al. [5]. In this model,

66 the raindrops with perfectly spherical shapes in the simulated rain event are assumed to be
67 distributed randomly in the spatial domain. However, the raindrops in the falling rain have a
68 complex mutual interaction with their neighbors, which causes varied velocity, sizes, and shapes,
69 as well as inflation, destabilization and ultimate fragmentation during the falling [6]. For example,
70 different raindrop shapes exist, e.g., spherical, semi-oblate, and parachute forms for raindrops
71 diameter less than 2-mm, between 2 and 5 mm, and larger than 5 mm, respectively [7]. The
72 raindrop shapes are highly dynamic in response to coalescence or fragmentation and to
73 aerodynamic forces (e.g., distorting the raindrop to a burger-bun-like shape [8]). Additionally, the
74 terminal velocity, i.e., the highest velocity attainable by the raindrop falling through the air, is
75 affected by raindrop mass, humidity, temperature, and orography, as well as wind. Thus, it is a
76 very challenging task to simulate a realistic stochastic rain field considering all the aforementioned
77 factors.

78 Calculations of raindrop impact pressure and/or impact stress is an important step before
79 evaluating the fatigue damage due to rain erosion. Due to its explicit formulation, the water
80 hammer pressure is viewed in literature (e.g., [7-11]) as a preliminary metric to evaluate the
81 raindrop impact force on solid surface. To consider the influence of the stress wave reflections,
82 Eisenberg et al. corrected the water hammer pressure by multiplying a term including impedance
83 of the substrate and the coating material [9]. By integrating the stochastic rain texture model and
84 the raindrop impact pressure profiles [5], Amirzadeh et al. further conducted the transient stress
85 analysis in a composite WTB using finite element analysis, although the stress analysis is limited
86 to the time period before which surface roughening starts to appear (i.e., the incubation period)
87 [11]. To the authors' knowledge, there is still a lack of an efficient and accurate computational
88 model that well reveals the complex fatigue mechanism for crack propagation induced by the

89 raindrop impact.

90 In the fatigue analysis, very few research has considered the influence of complex rain-
91 induced stress on the fatigue life-cycle of WTB coating, including the incubation period, the mass-
92 loss-rate (MLR) increasing period, and the placid period [12] , as shown in Fig. 1. The WTB
93 coating fatigue damage is initiated in the erosion incubation period and increased rapidly in the
94 MLR increasing period. In the erosion incubation period, the coating surface is smoother without
95 obvious pits and cracks, and there is no obvious observable mass loss due to raindrop erosion. The
96 damage in this period is mainly attributed to fatigue of the solid material under direct deformation
97 and stress wave propagation [13]. As the erosion process continues and the surface roughness is
98 increased in the MLR increasing period, the lateral jetting and hydraulic penetration produce large
99 shear stress on the surface and the fatigue crack opening causing the increased MLR [14]. In the
100 placid period, as the surface roughness is severely increased, liquid material accumulates on the
101 surface and reduces the impact damage of the oncoming raindrops resulting in a decreased MLR
102 in this period [5]. It is important to correctly estimate the time lengths of the former two periods
103 before the aerodynamic and structural performance of WTBs are significantly degraded. Although
104 several studies have investigated the WTB rain erosion considering the incubation period (e.g., [8,
105 9, 11]), very few have considered both the erosion incubation period and the MLR increasing
106 period. For example, the Miner's rule has been often applied to estimate the fatigue damage by a
107 simple linear accumulation of fatigue damage due to each stress cycle in the erosion incubation
108 period (e.g., [8-11, 15]). Eisenberg et al. [9] derived an analytic wind turbine LEE model and found
109 that fatigue damage rate is proportional to the impact velocity and rain intensity to the power of
110 6.7 and 2/3, respectively. However, in this model, the rain consists of only droplets of the median
111 diameter under a certain rain intensity, and the fatigue calculation only considers the crack

112 initiation during the erosion incubation period.

113 In view of existing challenges, the current paper presents a comprehensive computational
114 framework (Fig. 2) for analyzing the WTB coating fatigue induced by raindrop impact. The
115 framework investigates the WTB coating fatigue life and includes three parts: 1) an extended
116 stochastic rain field simulation, 2) raindrop-impact stress calculation, and 3) coating fatigue
117 analysis, as schematically shown in Fig. 3. The novelties of this work are three-fold:

- 118 1) An extended stochastic rain field simulation model considering the varied raindrops shapes
119 (spherical, flat, and spindle) and realistic raindrop size and distribution based on historical rain
120 data;
- 121 2) An efficient and accurate method to calculate the raindrop-impact stress under a stochastic rain
122 event using the smooth particle hydrodynamics (SPH) and a stress interpolation scheme;
- 123 3) Coating fatigue analysis including the erosion incubation period and the MLR increasing
124 period due to impact of raindrops.

125 The remainder of the paper proceeds as follows. Section 2 presents the detailed
126 methodologies of the proposed computational framework. Section 3 provides a case study using
127 the framework, followed by the results and discussion in Section 4. Section 5 gives the concluding
128 remarks, limitations, and future work.

129 **2 METHODOLOGIES**

130 Different from the existing simulated rain fields which only include perfectly spherical
131 raindrops (e.g., by the methods in [5]), the extended stochastic rain fields herein consists of
132 spherical and elliptical raindrop shapes according to the work in [16]. Since the raindrop impact
133 velocity is dominated by wind turbine rotation [5, 17], we consider the angle between the falling

134 raindrops and the rotating blade as the impact angle, instead of using the commonly assumed
 135 vertical hitting angle of 90 degrees [11, 15]. The raindrop impact stress is calculated using SPH
 136 and the FEA methods. To simulate the coating erosion in the life cycle of the blade, the coating
 137 fatigue analysis includes both fatigue incubation and crack propagation periods.

138 **2.1 Extended Stochastic Rain Field Simulation**

139 The extended stochastic rain field model is based on the stochastic rain texture model
 140 described in [5], and further considers different raindrop impact speeds, impact angles, sizes of
 141 raindrops, and shapes of raindrops in the simulated rain fields. The simulated stochastic rain field
 142 consists of three key components, including the number of raindrops in unit volume, the
 143 distribution of the size of raindrops, and the spatial distribution of raindrops with varying shapes
 144 in the simulated volume. The number of raindrops in unit volume V , $N(V)$, follows a Poisson
 145 distribution expressed as [5]:

$$146 \quad P(N(V) = k) = \frac{(\lambda V)^k e^{-\lambda V}}{k!} \quad (1)$$

147 where λ is the expected number of raindrops per unit volume, and $P(N(V) = k)$ is the probability of
 148 having k raindrops in volume V . Based on the relationship between the volume of water in air and
 149 the rain intensity suggested by Best [18], the expected number λ of raindrops per unit volume can
 150 be described by a power-law relationship with the rain intensity following Amirzadeh et al. [5]

$$151 \quad \lambda = 48.88I^{0.15} \quad (2)$$

152 where I is the rain intensity in mm h^{-1} . We use Best's drop size distribution [18] to connect the rain
 153 intensity with the distribution of the size of raindrops since it closely matches the experimental
 154 data [5]. The cumulative distribution function F of the raindrop size (e.g., diameter) is expressed

155 as:

$$156 \quad F = 1 - \exp \left[- \left(\frac{d}{1.3I^{0.232}} \right)^{2.25} \right] \quad (3)$$

157 where d is the raindrop diameter in mm and I is the rain intensity in mm h^{-1} .

158 Due to surface tension and external forces (e.g., aerodynamic force and gravity force),
 159 raindrops normally have varying shapes when impacting WTBs. In this paper, the equilibrium
 160 shape of raindrops is described by the axis ratio α , ratio of the minor axis to the major axis of the
 161 ellipse [16]. In the measurements by Beard et al., the axis ratio α of a raindrop is found to have a
 162 linearly decreasing relationship with the equivalent spherical radius r_0 (r_0 is in the range of 0.5 –
 163 4.5 mm), which is expressed as [16]

$$164 \quad \alpha = 1.030 - 0.124r_0 \quad (4)$$

165 To address the varying raindrop shapes in a rain event, the equivalent spherical radii r_0 of the
 166 simulated raindrops are obtained based on the Best's drop size distribution (Eq. 3). Three types of
 167 raindrop shapes are considered, perfect sphere, flat ellipsoid, and spindle ellipsoid. The flat-
 168 ellipsoid raindrops have the longest axis in horizontal plan, while the spindle-ellipsoid raindrops
 169 have the longest axis perpendicular to the horizontal plan. The horizontal cross-sectional area of
 170 both flat and spindle raindrops is assumed to be a circle, and the vertical cross-sectional area is an
 171 ellipse. The axis ratio of the minor axis to the major axis of the ellipse is calculated by Eq. (4). For
 172 the raindrops having the same equivalent spherical radius, their volumes are the same although
 173 their shapes may be different. In the experiments of McTaggart-Cowan and List (1975) [16, 19],
 174 raindrop collisions were used to classify three predominate breakup types which is neck (27%),
 175 sheet (55%) and disk (18%). As the raindrop shapes after collision of these three types are

176 comparable to the flat ellipsoid, spindle ellipsoid, and perfect sphere [16, 19], we select the same
177 probability of occurrence for the three raindrop shapes to be 27%, 55%, and 18%, respectively, in
178 the simulated stochastic rain event, as shown in Fig. 4.

179 Due to the WTB rotation and complex weather condition (e.g., wind effect), raindrops could
180 impact the WTB at different angles (Fig. 4). The normal and tangential loads exerted due to
181 perpendicular impact and inclined impact, respectively, could create different stress distribution in
182 the blade coating. Thus, this paper further considers the inclined impact angle between the rotating
183 blade and the falling raindrops. While the impact angle could range from 0 to 180° (denoted as [0,
184 180°] herein) as demonstrated in Fig. 4, in this paper it is assumed to follow a uniform distribution
185 from 0 to 90° considering the symmetric impacting effect between the ranges of [0, 90°] and [90°,
186 180°].

187 As a raindrop is falling, the air resistance applied on the raindrop approaches to its gravity,
188 which may result in a constant terminal speed. For instance, the terminal speed of raindrops with
189 diameters larger than 3.5 mm through stagnant air is approximately 9 ms⁻¹ [17, 20]. However, as
190 a result of the high relative speed between a rotating megawatt-scale WTB and the falling
191 raindrops, raindrop impact speed at the tip of the blade could be 90-100 ms⁻¹ [17]. In addition, the
192 raindrops are considered as uniformly distributed in a tall-column volume. The height h of the
193 column is calculated by the multiplication of the impact speed v and the duration T of the simulated
194 rain event (i.e., $h = v \times T$), as also conducted by Amirzaadeh et al. [5]. Given the statistical data of
195 rainfall history at a wind turbine location (see Section 3 for instance), the probability mass function
196 (PMF) of the rain intensity can be obtained and used to determine different rainfall hours per year
197 for the coating fatigue life estimation in Section 2.3.

198 **2.2 Method for Raindrop Impact Stress Calculation**

199 The raindrop impact is simulated by the transient SPH using the FEA tool in
200 ABAQUS/Explicit [11]. This SPH approach has three merits: (1) taking into the account of large
201 deformation of raindrops during impact on the solid, (2) directly calculating the transient stress
202 time series, and (3) characterizing the impact wave propagation in the FEA model.

203 **2.2.1 Impact stress calculation of a single raindrop**

204 The SPH approach is particularly effective to solve large deformation problems that can
205 afford moderate computational cost, which is its key advantage over traditional FEA and the
206 coupled Eulerian-Lagrangian approaches. The former is not accurate for large deformation
207 analysis, while the latter is usually more computationally expensive than SPH. Detailed theory and
208 application of SPH can be found in literature [21-23]. Keegan et al. [24] utilized the SPH method
209 to simulate the effects of rain and hail on the coating materials of wind turbines. The SPH method
210 is coupled with traditional FEA to study the fluid-structural interaction between the raindrop and
211 the WTB (e.g., Astrid et al. [25] and Verma et al. [26]).

212 To reflect the aforementioned complexity of raindrops in a rain event, herein the SPH analysis
213 is first applied to investigate single raindrop impact considering different raindrop sizes, raindrop
214 shapes, impact speeds, and impact angles. Specifically, we conduct varying single-raindrop impact
215 cases considering 9 raindrop sizes (equivalent diameter $d = 1, 2, 3, 4, 5, 6, 7, 8, 9$ mm), 3 raindrop
216 shapes (flat, spindle, spherical), 6 impact angles ($\theta = 15^\circ, 30^\circ, 45^\circ, 60^\circ, 75^\circ, 90^\circ$), and 5 impact
217 speeds ($70 \text{ ms}^{-1}, 80 \text{ ms}^{-1}, 90 \text{ ms}^{-1}, 100 \text{ ms}^{-1}, 110 \text{ ms}^{-1}$). Detailed results and discussion are seen
218 in Section 4.2. The von Mises stress due to multiple-raindrops impact in a simulated rain field is
219 further calculated based on the interpolation of the von Mises stress results of the single-raindrop
220 impact cases, as explained in the following section.

221 **2.2.2 Impact stress calculation under a random rain event**

222 In a real rain event, a significant number of raindrops with varied sizes, shapes, and impact
223 speeds and angles are randomly impacting on WTBs. For a single raindrop impact simulation by
224 SPH, it costs 2 hours using a computer (Intel(R) Core(TM) i7-8750H CPU @ 2.20 GHz Processor,
225 Memory (RAM) 32 GB, 64-bit Windows Operating System). Thus, it is not practical to conduct
226 SPH simulation for all raindrops in a rain event. Instead, an interpolation method is proposed to
227 efficiently obtain the impact stress due to varied raindrop sizes, shapes, and impact speeds and
228 angles. The method utilizes pre-calculated impact stress from the single-raindrop impact cases.
229 Detailed steps are explained as follows:

230 **Step 1:** Create a stochastic rain field by the method presented in Section 2.1 given a rain
231 intensity and a rain duration.

232 **Step 2:** Obtain the impact stress of a random raindrop by interpolating the SPH impact stress
233 from the single-raindrop impact cases in Section 2.2.1. After identifying the size, shape, and the
234 impact angle and speed of the random raindrop, a circular domain with the impact point as the
235 center and 10 times of the raindrop equivalent diameter as the radius is considered as the area
236 influenced by the raindrop impact [11]. Then, choose the same type of raindrop shape, and
237 interpolate the stress in this circular area according to the stress results of the calculated impact
238 cases that have the closest raindrop diameter, impact angle, and impact speed.

239 **Step 3:** Repeat Step 2 for calculating the impact stress due to the other random raindrops.
240 Since the time interval between two consecutive raindrops impact is almost three orders of
241 magnitude longer than the time required for the stress wave generated by a single raindrop impact
242 to disappear [11], we assume that the stress waves from different single-raindrop impacts will not
243 interact with each other.

244 Through the above steps, the complex stress state under a stochastic rain field can be
245 calculated and used for the coating fatigue analysis as follows.

246 **2.3 Coating Fatigue Analysis**

247 Herein we first use the traditional alternating stress (S) versus the number of cycles to failure
248 (N), here defined as the stress life (S-N) method to calculate the lasting time of the incubation
249 period, then propose a fatigue crack propagation method to calculate the fatigue damage during
250 the MLR increasing period.

251 **2.3.1 Fatigue analysis for the erosion incubation period**

252 The traditional S-N method has been widely used to calculate the fatigue life during the
253 incubation period [11, 27, 28]. The S-N curve formula is expressed as:

$$254 \quad \sigma_a = \sigma_f (N_f)^b \quad (5)$$

255 where σ_f is the fatigue strength coefficient (FSC), and b is the fatigue strength exponent (FSE),
256 N_f is the number of allowable cycles under a stress amplitude σ_a . According to the fatigue
257 experiments in [29], the values of σ_f and b in Eq.(5) are 83.3MPa and -0.117 , respectively, for the
258 epoxy coating in this paper.

259 It is worth noting that the S-N curve formula differs at different stress ratios R which equal
260 the ratio of the minimum cyclic stress to the maximum cyclic stress (i.e., $R = \sigma_{\min} / \sigma_{\max}$). However,
261 due to the lack of fatigue experimental data for the coating material under different stress ratios,
262 the constant life diagram, which requires multiple S-N curves at varying stress ratios, cannot be
263 created in this paper. In order to implement the one S-N curve based on the fatigue experiments in
264 [29], the stress amplitudes are corrected according to the Goodman's equation [11]:

$$265 \quad \sigma_a' = \frac{\sigma_a UTS}{UTS - \sigma_m} \quad (6)$$

266 where σ_a' is the corrected amplitude, σ_m is the mean stress, and UTS is the ultimate tensile
 267 strength. The UTS of the epoxy material ($UTS = 73.3\text{MPa}$) from [29] is used in this paper.
 268 Substituting the σ_a in Eq. (5) by σ_a' , the number of allowable stress cycles N_f can be calculated
 269 as

$$270 \quad N_f = \left(\frac{\sigma_a'}{\sigma_f} \right)^{1/b} \quad (7)$$

271 In Eq. (7), the cyclic stress should be a constant-amplitude cyclic stress, but the actual
 272 impact stress has varied stress amplitudes due to the randomness of raindrop impact. In order to
 273 have cycle-by-cycle fatigue analysis, a simple-range counting method [30] is applied to count all
 274 the half cycles, i.e., the local maximum (minimum) stress and the neighboring minimum
 275 (maximum) stress are selected to constitute a half stress cycle. In this way, the complex stress
 276 curve is split into half-cyclic stresses with varying constant-amplitudes and the N_f in Eq. (7) is
 277 calculated for each half-cycle. Different from the rainflow cycle counting that breaks the stress
 278 cycle sequence, the simple-range counting method could sequentially calculate fatigue damage for
 279 each half-cycle. As a result, the fatigue damage D under half-cyclic stresses is linearly accumulated
 280 based on the Miner's rule

$$281 \quad D = \sum_i \frac{0.5}{N_f^i} \quad (8)$$

282 The fatigue life of the erosion incubation period is then calculated as

$$283 \quad t_{\text{incubation}} = \frac{t_s}{D_s} \quad (9)$$

284 where t_s is the duration of the simulated rain and D_s is the damage accumulated over time t_s .

285 **2.3.2 Fatigue analysis for the mass-loss-rate increasing period**

286 The MLR increasing period starts at the end of the incubation period when the surface
 287 roughness increases severely [5]. According to the crack propagation law [31], we use the obtained
 288 raindrop impact stress from Section 2.2.2 to calculate the crack depth, and use a crack-propagation
 289 stability criterion to calculate the fatigue life of the MLR increasing period when the rain intensity
 290 is larger than a threshold. When the rain intensity is smaller than or equal to the threshold, the
 291 computational time using this traditional crack propagation method is increased significantly. For
 292 example, using the traditional crack propagation method, the computer in this study will take
 293 approximately 245 days to simulate a fatigue life of 11462 hours when the rain intensity equals to
 294 5 mm h⁻¹. To overcome the computational burden, an equivalent crack propagation method is
 295 proposed for estimating the total crack propagation time by calculating the equivalent stress
 296 amplitude, when the rain intensity is smaller than a threshold. In this study, the rain intensity
 297 threshold is selected to be 10 mm h⁻¹ based on our current affordable computational time. The
 298 proposed equivalent crack propagation method significantly reduces the computational time when
 299 calculating fatigue life for the MLR increasing period. For instance, it only cost 5 minutes to
 300 simulate the same fatigue life when the rain intensity equals to 5 mm h⁻¹.

301 The crack propagation method is first explained. Fatigue crack propagation studies are
 302 performed with the cyclic-crack-tip stress state determined by a stress intensity factor range ΔK .
 303 According to the Paris law [31], the crack growth rate is expressed as:

$$304 \quad \frac{da}{dN} = C(\Delta K)^m \quad (10)$$

305 where C and m are the basic parameters describing the fatigue crack growth performance of the
 306 material, obtained from the crack growth experiments. According to Brown's experimental results
 307 [32], the crack propagation test for the epoxy material (i.e., the gelcoat of a WTB) determines these
 308 parameters to be $C=9.7$ and $m=0.08$. Considering that the von Mises stress is used in the fatigue
 309 analysis (i.e., $R = \frac{\sigma_{min}}{\sigma_{max}} > 0$), the stress intensity factor range ΔK is expressed as [27, 28]

$$310 \quad \Delta K = K_{max} - K_{min} \quad (11)$$

311 The calculation formula of stress intensity factor K is expressed as [27, 28]

$$312 \quad K = Y\sigma\sqrt{\pi a} \quad (12)$$

313 Therefore, the maximum stress intensity factor K_{max} and the minimum stress intensity factor K_{min}
 314 can be expressed as $K_{max} = Y\sigma_{max}\sqrt{\pi a}$ and $K_{min} = Y\sigma_{min}\sqrt{\pi a}$, respectively. Y is a dimensionless
 315 parameter related to the shape of the crack. a is the crack depth.

316 For a constant amplitude stress and the number of stress cycles N is small, the change in crack
 317 depth a is small and the stress intensity factor range ΔK is viewed as a constant. Thus the crack
 318 growth rate (Eq. (10)) under a constant-amplitude cyclic stress can be considered as a constant. As
 319 a result, the crack depth formula is approximately as

$$320 \quad a = a_0 + \int_0^N C(\Delta K)^m dN = a_0 + N \times C(\Delta K)^m \quad (13)$$

321 where N is the number of applied stress cycles and a_0 is the initial crack depth, which is selected
 322 to be 12 μm according to the range of surface roughness (5 to 20 μm) used in [33]. This surface
 323 roughness range is viewed as the indicator of the start of the MLR increasing period in this paper.

324 Since the stress time series have been split into half-cycle stresses, each half-cycle stress curve
 325 is viewed as a constant amplitude stress with the number of stress cycles 0.5 ($N = 0.5$). The crack
 326 depth a_{i+1} after one half-cycle stress cycle is calculated based on Eqs. (11) - (13)

$$327 \quad a_{i+1} = a_i + 0.5 \times C \left[Y(\sigma_{\max} - \sigma_{\min}) \sqrt{\pi a_i} \right]^m \quad (14)$$

328 According to the elastic fracture criterion, when the maximum stress intensity factor K_{\max} is
 329 greater than the fracture toughness K_C , the crack extends in a rapid (unstable) manner without an
 330 increase in load or applied energy [27]. Here the fracture toughness of the epoxy material is $K_C =$
 331 $0.59 \text{ MPa m}^{1/2}$ [32]. Here the relationship $K_{\max} > K_C$ is viewed as the first criterion indicating the
 332 crack propagation has been completed. In addition, when the crack depth is greater than the coating
 333 thickness, it also indicates that the crack propagation has been completed. By satisfying either the
 334 aforementioned two criteria, the duration of the MLR increasing period t_{MLR} is obtained.

335 However, when the rain intensity is low, the time required for iteratively calculating the crack
 336 depth (Eq. (14)) till the end of the crack propagation is significantly large due to the relatively
 337 small impact stress. Herein for low rain intensity (i.e., $I \leq 10 \text{ mm h}^{-1}$), an average stress amplitude
 338 $\Delta\sigma$ is first calculated as an equivalent constant-amplitude stress with the same applied number of
 339 cyclic stresses during the simulated rainfall time, which is based on the Paris formula. Then obtain
 340 the fatigue life based on accumulation of fatigue damage of multiple simulated times. Details of
 341 this equivalent crack propagation method are provided as follows.

342 Based on Eqs. (10) and (12), the number of allowable cyclic stress N_c can be calculated as:

$$343 \quad N_c = \int_0^{N_c} dN = \int_{a_0}^{a_c} \frac{da}{C(Y\Delta\sigma\sqrt{\pi a})^m} = \frac{1}{C(Y\Delta\sigma\sqrt{\pi})^m} \int_{a_0}^{a_c} \frac{da}{a^{m/2}} \quad (15)$$

344 If $m \neq 2$

$$345 \int_{a_0}^{a_c} \frac{da}{a^{m/2}} = \frac{a_c^{\left(1-\frac{m}{2}\right)} - a_0^{\left(1-\frac{m}{2}\right)}}{-m/2+1} \quad (16)$$

346 If $m = 2$

$$347 \int_{a_0}^{a_c} \frac{da}{a} = \ln\left(\frac{a_c}{a_0}\right) \quad (17)$$

348 The calculation formula of fatigue life is derived as [27, 28]

$$349 N_c = \begin{cases} \frac{2}{(m-2)C(Y\Delta\sigma\sqrt{\pi})^m} [a_0^{\left(1-\frac{m}{2}\right)} - a_c^{\left(1-\frac{m}{2}\right)}], & m \neq 2 \\ \frac{1}{C(Y\Delta\sigma\sqrt{\pi})^m} \ln\left(\frac{a_c}{a_0}\right), & m = 2 \end{cases} \quad (18)$$

350 The parameters of the calculation formula of fatigue life (C, m, Y, a_0) are constant. Based on
 351 Eq.(18), the average stress amplitude $\Delta\sigma$ of N number of varied-amplitude cyclic stress can be
 352 calculated as

$$353 \Delta\sigma = \begin{cases} \left\{ \frac{2}{N(m-2)C(Y\sqrt{\pi})^m} \left[a_0^{\left(1-\frac{m}{2}\right)} - a_c^{\left(1-\frac{m}{2}\right)} \right] \right\}^{\frac{1}{m}}, & m \neq 2 \\ \left[\frac{1}{CN(Y\sqrt{\pi})^m} \ln\left(\frac{a_c}{a_0}\right) \right]^{\frac{1}{m}}, & m = 2 \end{cases} \quad (19)$$

354 where N is the applied number of cyclic stress and a is the crack depth. By Eq. (12), the critical
 355 crack depth can be obtained by setting K_{\max} equal to the fracture toughness K_C [27, 28]:

$$a_c = \left(\frac{K_c}{Y\sigma_{\max}} \right)^2 / \pi \quad (20)$$

where σ_{\max} is the maximum stress under one simulated rainfall time period t .

The obtained average stress amplitude $\Delta\sigma$ and the critical crack depth a_c are then substituted into Eq. (18) to calculate the number of allowable cyclic stress N_c . Assuming the fatigue damage is linearly accumulated for multiple simulated rainfall times, the duration of the MLR increasing period under low rain intensities can be calculated as

$$t_{MLR} = \frac{N_c}{N_t} t \quad (21)$$

where N_c is the allowable number of stress cycles till the end of crack propagation under low rain intensities, N_t is the applied number of stress cycles in one simulated rainfall time t . Accuracy results when using this approximation for calculating fatigue life under low rain intensities are discussed in Section 4.3.

2.3.3 Fatigue life calculation for wind turbine blade coating

The total fatigue life, t_I , under a rain intensity at each element of the FEA model is calculated by adding the fatigue life of the erosion incubation period and the fatigue life of the MLR increasing period, expressed as

$$t_I = t_{incubation} + t_{MLR} \quad (22)$$

where $t_{incubation}$ and t_{MLR} are obtained by Eqs. (9) and (21), respectively. In the studied WTB coating, as the crack grows, adjacent crack tips may interact with each other causing that the crack propagation path bends and the cracks merge. According to Li et al. [34], when the cracked

375 area accounts for 78% ~ 90% of a coating material, the cracks start to merge and the coating
 376 enters into a rapid failure stage. Here, the 84th percentile (center of the 78% to 90% from Li et al.
 377 [34]) of the total fatigue life of all FEA elements is selected as the fatigue life of the WTB
 378 coating.

379 Combining the PMF P_I of the rain intensity and the total rainfall hours per year t_A at a WT
 380 location, the accumulated fatigue damage of the WTB coating per year $D_{1\text{year}}$ considering different
 381 rain intensities can be calculated as

$$382 \quad D_{1\text{year}} = \sum_I \frac{P_I \times t_A}{t_I} \quad (23)$$

383 Thus, the expected fatigue life t_f of the WTB coating can be calculated as

$$384 \quad t_f = \frac{1}{D_{1\text{year}}} \quad (24)$$

385 **3 CASE STUDY**

386 The proposed computational framework is applied in the fatigue life evaluation of a
 387 composite panel at the tip section of a blade leading edge. The composite panel is modelled in the
 388 FEA analysis as a layup that consists of a coating layer, a composite layer beneath the coating
 389 layer, a foam core material layer in the middle, and another composite layer at the bottom (Fig. 5).
 390 The coating material is an epoxy gelcoat, as specified in the Sandia 100-meter all-glass baseline
 391 WTB [35] and has a thickness of 0.6 mm. Each composite layer consists of the composite material
 392 QQ1, which is a glass-fiber-reinforced plastic (GFRP) laminate that consists of Vantico TDT 177-
 393 155 Epoxy Resin, Saertex U14EU920-00940-T1300-100000 0's, and VU-90079-00830-01270-
 394 000000 45's fabrics [36]. The core material is selected to be CorecellTM M-Foam M200 [37].
 395 Detailed material properties are provided in Table 1.

396 The dimension of the simulated blade panel is $100 \times 100 \times 15.6$ mm. The boundary condition
397 is set to fixing the bottom surface of the panel as a typical approach for raindrop impact simulation
398 [11, 26]. Two assumptions are made here: 1) the layers in the sandwich panel are perfectly bonded,
399 as the consideration of cohesive property between layers would complicate the stress analysis; 2)
400 the effect of the blade surface curvature on the impact stress is not considered in this case study.
401 There are 10000, 50000, and 50000 SC8R elements are used to mesh the coating layer, each of the
402 composite layer, and the foam layer, respectively (Fig. 5). SC8R is an 8-node, quadrilateral, first-
403 order interpolation, stress/displacement continuum shell element with reduced integration. The
404 average mesh size of the SPH particles in a raindrop is 0.1 times the diameter of the raindrop. The
405 total number of SPH particles is $\sim 750 - 1100$ depending on different raindrop sizes and shapes.
406 These numbers of the SC8R elements and the SPH particles are determined based on the sensitivity
407 analyses of different mesh sizes on the calculated stress results and the affordable computational
408 time in this case study.

409 The proposed computational framework is validated by comparing the fatigue life of the
410 studied WTB tip panel under different rain intensities with Bech's results in [8] with the same
411 impact speed of 90 ms^{-1} . In addition, based on the rainfall statistics data in Miami, FL, from August
412 1957 to August 1958 [38], the PMF of the rain intensity is created (see Figure 6) and used to
413 calculate the fatigue life of the studied panel. Detailed results and discussion are provided as
414 follows.

415 **4 RESULTS AND DISCUSSION**

416 **4.1 Extended Stochastic Rain Fields**

417 As a demonstration, Fig. 7 shows the top views of the extended stochastic rain fields with

418 varying raindrop shapes and sizes under four rain intensities, 1 mm h⁻¹, 10 mm h⁻¹, 20 mm h⁻¹, and
419 50 mm h⁻¹. The flat ellipsoid, spindle ellipsoid, and spherical raindrops are indicated by red, green,
420 and blue solid circles, respectively. This figure clearly visualizes that as the rain intensity increases
421 the number and the size of raindrops increase accordingly. Because this research focuses on the
422 WTB coating stress and fatigue due to the raindrop impact, as elaborated in Sections 4.2 and 4.3,
423 the complex mutual interaction and dynamic deformation of raindrops during their falling are not
424 considered here.

425 **4.2 Raindrop Impact Stress**

426 The stress waves due to raindrop impact is first investigated. Figures 8 and 9 demonstrate the
427 propagation of von Mises stress of the panel under a single spherical raindrop impacting at the
428 panel center with 90° impact angle. The raindrop diameter is 2 mm, and the impact speed is 90
429 ms⁻¹. As a result of the impact, there is a Rayleigh wave generated and propagated from the impact
430 center to the free boundary of the coating surface (Fig. 8). In addition, the impact produces
431 longitudinal and transverse body waves that accompany stress variation inside the panel exhibiting
432 an interference field of these waves (Fig. 9).

433 Two high-stress regions are observed during the raindrop impact process: the one occurring
434 at the raindrop-coating contact surface (Figs. 8(b-f)) and the other is propagating through the
435 thickness below the surface (Figs. 9(a-f)). The former is due to the raindrop peak impact pressure
436 acting as the primary wave source, while the latter is caused by superposition of the stresses
437 initiated from the shock wave front in the raindrop and from the high-pressure point. These
438 findings further confirm that micro-crack/fatigue is possibly occurring both at the raindrop-coating
439 contact surface and underneath the coating.

440 It is worth noting that there is a clear stress interface between the QQ1 layer and the foam
441 layer (Figs. 9(b-f)) due to the different elastic material properties of the two layers. Under the
442 assumption of perfectly bonded layers, the elastic deformation of QQ1 and foam layer is the same
443 in the interfaces between layers. As the Young's modulus of the foam layer is much lower than
444 that of the QQ1 layer (see Table 1), the stresses in the foam layer are much lower than those in the
445 QQ1 layer. This finding confirms that the foam layer plays a vital role as a stress cushion in
446 composite WTBs.

447 The influence of the raindrop size, impact speed, impact angle, and raindrop shape on the
448 stress evolution on the impacted coating is shown in Fig. 10. The coating center element with the
449 highest von Mises stress is studied here. Figure 10(a) shows the von Mises stress induced by the
450 normal impact (90°) under the same impact speed (90 ms^{-1}) and different spherical raindrop
451 diameters (1 mm, 2 mm, and 5 mm). A clear two-peak mode is observed for the stress time series
452 of all three cases, which is in line with earlier observations [5]. The gap between the two peaks is
453 increased as the raindrop size increases (Fig. 10(a)). The first stress peak is due to the direct impact
454 of the raindrop against the coating surface, while the second stress peak may be generated by the
455 shock wave front after the high density liquid region is created [39].

456 Figure 10(b) compares the von Mises stress under the normal impact (impact angle 90°) of a
457 spherical raindrop (diameter 2 mm) with three different impact speeds (70 ms^{-1} , 90 ms^{-1} , and 100
458 ms^{-1}). It is found that three first stress peaks (44 MPa, 64 MPa, and 86 MPa) increase as the impact
459 speed increases. The ratio among the three first-peak von Mises stresses is approximately closed
460 to the ratio among the square of the impact speeds, which is consistent with the relationship
461 between the kinetic energy and the impact speed of the raindrop. However, the second stress peak
462 is not significantly influenced by the impact speed as shown in Fig. 10(b).

463 To investigate the influence of the impact angles on the stress, a spherical raindrop with
464 diameter of 2 mm and impact speed of 90 ms^{-1} is used to impact the blade panel with three different
465 impact angles (30° , 60° , and 90°). Figure 10 (c) shows that, as the impact is inclined, the stress is
466 dramatically reduced, especially for the first peak stress, which indicates that non-perpendicular
467 raindrop impact could significantly reduce the impact stress.

468 Figure 10(d) compares the von Mises stress under three different raindrop shapes (flat,
469 spindle, spherical) with the same volume ($\frac{4}{3}\pi \times 4^3 \text{ mm}^3$) and the impact speed (90 ms^{-1}). For the
470 non-spherical raindrops (spindle and flat), the two stress peaks are not as obvious as those due to
471 the spherical raindrop. Instead, the stress corresponding to the non-spherical raindrops have a large
472 fluctuation in the time series. In addition, the spindle raindrop creates the maximum first-peak and
473 longest fluctuating time among the three raindrop shapes, while the flat raindrop generates smaller
474 stress fluctuation than those by the other two counterparts, as demonstrated in Fig. 10(d).

475 The accuracy of the stress interpolation method proposed in Section 2.2.2 is verified by
476 comparing the interpolated impact stress with the stress directly calculated using the SPH
477 approach. As a demonstration, Fig. 11 shows an interpolated stress when a 2.5 mm diameter
478 spherical raindrop impact at the top-right corner of the blade panel with an impact angle of 80°
479 and an impact speed of 90 ms^{-1} . Taking the center of the panel as the origin of the coordinate
480 system, the impact point is at (28 mm, 28 mm). The four closest cases are (spherical, $d = 2 \text{ mm}$, θ
481 $= 75^\circ$, $v = 90 \text{ ms}^{-1}$), (spherical, $d = 2 \text{ mm}$, $\theta = 90^\circ$, $v = 90 \text{ ms}^{-1}$), (spherical, $d = 3 \text{ mm}$, $\theta = 75^\circ$, $v =$
482 90 ms^{-1}) and (spherical, $d = 3 \text{ mm}$, $\theta = 90^\circ$, $v = 90 \text{ ms}^{-1}$). Figure 11(a) compares the time series of
483 interpolated von Mises stress of the raindrop and those of the closes four raindrop impact cases.
484 As illustrated in Fig. 11(b), it is observed that the interpolated stress agrees well with the stress
485 directly calculated by the SPH approach.

486 4.3 Blade Coating Fatigue

487 The accuracy of the proposed equivalent crack propagation method is first verified by
488 comparing fatigue life of the MLR increasing period based on the equivalent crack propagation
489 method and the traditional crack propagation method, as shown in Table 2. Under large rain
490 intensities ($11 \text{ mm h}^{-1} \leq I \leq 20 \text{ mm h}^{-1}$), the relative error using the equivalent crack propagation
491 method is less than 3% and decreases as the rain intensity decreases. The smallest relative error
492 using the equivalent crack propagation method when rain intensity equals to 11 mm h^{-1} is only
493 0.06%. Therefore, when the rain intensity is low (i.e., $I \leq 10 \text{ mm h}^{-1}$ in this paper), the equivalent
494 crack propagation method could indeed produce fatigue life of the MLR increasing period as
495 accurate as the traditional crack propagation method.

496 The influence of the rain intensity, raindrop impact speed, raindrop impact angle, and
497 raindrop shape on fatigue life are investigated. The fatigue life of the incubation period, the MLR
498 increasing period, and the total fatigue life (summation of the incubation period and the MLR
499 increasing period) under different rain intensities, raindrop impact speeds, raindrop impact angles,
500 and raindrop shapes are provided in Table 3 and depicted in Fig. 12.

501 Figure 12(a) compares the fatigue life of the blade coating under the same vertical impact
502 (impact angle = 90°), the impact speed of 90 ms^{-1} , and the spherical raindrops with five different
503 rain intensities (1 mm/h, 5 mm/h, 10 mm/h, 15 mm/h, and 20mm/h). As expected, the fatigue life
504 of the coating decreases exponentially with the increase of the rainfall intensity. It is interesting to
505 find that under low rain intensity (e.g., $I < 7\sim 8 \text{ mm/h}$) the incubation period is shorter than the
506 MLR increasing period, while it becomes longer than the MLR increasing period under large rain
507 intensity (e.g., $I \geq 10 \text{ mm/h}$). This is probably due to that severer impact stress, consequently
508 severer crack propagation, occurs under larger raindrop size (see Fig. 10(a)) and more raindrops

509 hitting at large rain intensity than that at small rain intensity. This finding also indicates that a rain
510 event with a large rain intensity could more detrimentally influence the blade coating crack
511 propagation than the crack initiation.

512 Figure 12(b) compares the fatigue life of the blade coating under the same rain intensity (5
513 mm/h) and the vertical impact (impact angle = 90°) of spherical raindrops with five different
514 impact speeds (70 ms^{-1} , 80 ms^{-1} , 90 ms^{-1} , 100 ms^{-1} , and 110 ms^{-1}). There is a significantly large
515 gap between the incubation period and the MLR increasing period at the impact speed of 70 ms^{-1} ,
516 which means the MLR increasing period dominates the total fatigue life under small impact speeds.
517 This gap is narrowed down as the impact speed increases. The current finding also indicates that
518 the raindrop impact speed influences the MLR increasing period severer than incubation period.

519 Figure 12(c) compares the fatigue life of the blade coating under the same rain intensity (5
520 mm/h) and impact speed (90 ms^{-1}) of spherical raindrops with five different impact angles (15° ,
521 30° , 45° , 60° , 75° , and 90°). The fatigue life of the MLR increasing period dominates the total
522 fatigue life under small impact angle. As the impact angle increases, both the fatigue life of the
523 incubation period and the MLR increasing period are exponentially decreasing.

524 Figure 12(d) compares the fatigue life of the blade coating under the same rain intensity (5
525 mm/h), impact speed (90 ms^{-1}) and the vertical impact (impact angle = 90°), but three different
526 raindrop shapes (flat, spherical, spindle). It is interesting to find that 1) under the flat raindrops the
527 MLR increasing period is 21.8 times longer than the incubation period; 2) the MLR increasing
528 period under the flat raindrops is 250.1 times longer than that under the spindle raindrops. These
529 could be probably because the spindle raindrops cause larger stress peak and longer stress
530 fluctuation than those caused by the flat raindrops (see Fig. 10(d)).

531 To further verify the accuracy of the proposed computational framework, the calculated total
532 fatigue life of the blade coating is compared with that obtained by Bech et al. [8] under the same
533 impact speed of 90 ms^{-1} . Table 4 compares the total fatigue life under five rain intensities (20 mm
534 h^{-1} , 10 mm h^{-1} , 5 mm h^{-1} , 2 mm h^{-1} , and 1 mm h^{-1}). In this table, the hours per year indicate the
535 number of hours corresponding to the rain intensity in a year, which is from Bech et al. [8]. The
536 fraction of life spent per year equals the hours per year divided by the calculated total fatigue life.
537 The reciprocal of the sum of fraction is obtained as the expected life in year. In general, the total
538 fatigue life under the five rain intensities are longer than those obtained by Bech et al. [8]. Using
539 the same rain hours per year data, the expected fatigue life using the proposed framework is 2.1
540 years which is slightly longer than that obtained by Bech et al. [8]. This longer fatigue life is mainly
541 because the proposed framework involves more sophisticated and realistic computational
542 approaches. For example, the extended stochastic rain field simulation considers various impact
543 angles and raindrop shapes that may alleviate the calculated stress compared with that obtained by
544 assumed vertical impact of all perfectly spherical and fixed-diameter raindrops used in Bech et al.
545 [8]. Given that very few WTB rain erosion experimental data are available in literature, this
546 comparison still shows that the proposed computational framework could produce reasonable
547 rain-erosion fatigue life for WTBs. It is worth noting that the fatigue life here is based on the
548 assumption that the blade is under continuous raindrop impact throughout its service life and can
549 be conservative.

550 Based on the rainfall statistics data in Miami, FL, from August 1957 to August 1958 [38],
551 the rain-erosion fatigue life of the Sandia 100-meter all-glass baseline WTB is ~ 1.3 years using
552 the proposed computational framework and the above expected fatigue life calculation method.
553 This indicates the necessity of the blade surface repairing as early as 1.3 years after installation.

554 **5 CONCLUSIONS**

555 For analyzing WTB coating fatigue due to rain erosion, this paper presents a state-of-the-art
556 computational framework that including an extended stochastic rain field simulation (considering
557 varied raindrop sizes, impact speeds, impact angles, and raindrop shapes), SPH-and-interpolation
558 hybrid raindrop impact stress calculation, and coating fatigue analysis (considering both the
559 erosion incubation period and the MLR increasing period for the first time). Based on this new
560 framework, some interesting results are obtained and summarized as follows:

- 561 1) Both surface Rayleigh wave and longitudinal and transverse body wave of impact stress are
562 generated by raindrop impact accompany with high-stress regions during the propagation of
563 these stress waves in the WTB.
- 564 2) The influence study of the raindrop size, impact speed, impact angle, and raindrop shape on
565 the stress evolution on the impacted coating shows that the inclined impact of flat-ellipsoid
566 raindrops could produce smaller stress fluctuation than the vertical impact of spindle-ellipsoid
567 raindrops do.
- 568 3) The proposed stress interpolation method and the equivalent crack propagation method could
569 efficiently and accurately calculate the impact stress and fatigue, respectively, under a
570 stochastic rain event.
- 571 4) The influence study of the rain intensity, impact speed, impact angle, and raindrop shape on
572 the fatigue life reveals that i) a rain event with a large rain intensity could more detrimentally
573 influence the blade coating crack propagation than the crack initiation; ii) the MLR increasing
574 period dominates the total fatigue life under small impact speeds (e.g., 70 m/s) and the raindrop
575 impact speed influences the MLR increasing period severer than incubation period; iii) the

576 vertical impact of spindle-ellipsoid raindrops could cause significantly larger fatigue damage
577 than the inclined impact of flat-ellipsoid raindrops do.

578 5) The proposed framework is verified by comparing the calculated fatigue life with existing
579 results in literature, and is readily applicable to predict WTB coating fatigue life due to rain
580 erosion given rainfall statistic data at a location.

581 Although the current research provides innovative contributions for predicting the WTB
582 coating fatigue life due to rain erosion, limitations and future work may include:

583 1) The usage of the proposed framework for WTB design and maintenance has not be investigated
584 in this paper. Future work may be the application of the framework to design of new WTB
585 coating and to optimal control of wind turbine operation to reduce the rain erosion for WTB.

586 2) The rain moisture effect, the chemical corrosion from insects, and other object impacts (e.g.,
587 atmospheric particles, hail, and sand) have not considered in this paper. WT damage
588 considering these factors, besides the rain erosion, is worth investigating in the future.

589

590 **REFERENCES**

- 591 1. Woods, R.D., *Screening of surface waves in soils*. J. Soil. Mech. Found. Div., 1968. **94**: p. 951-980.
- 592 2. Busch, H., G. Hoff, G. Langbein, Geoffrey Taylor, D. C. Jenkins, M. A. Taunton, A. A. Fyall, R. F. Jones,
593 and T. W. Harper., *Rain erosion properties of materials*. Philosophical Transactions for the Royal Society
594 of London. Series A, Mathematical and Physical Sciences, 1966. **1110**: p. 168-181.
- 595 3. Heymann, F.J., *High-speed impact beteen a liquid drop and a solid surface*. J. Appl. Phys., 1969. **40**: p.
596 5113-5122.
- 597 4. Dear, J.P. and J.E. Field, *High-speed photography of surface geometry effects in liquid/solid impact*. J.
598 Appl. Phys., 1988. **63**: p. 1015-1021.
- 599 5. Amirzadeh, B., et al., *A computational framework for the analysis of rain-induced erosion in wind turbine*
600 *blades, part I: Stochastic rain texture model and drop impact simulations*. Journal of Wind Engineering
601 and Industrial Aerodynamics, 2017. **163**: p. 33-43.
- 602 6. Villiermaux, E. and B. Bossa, *Single-drop fragmentation determines size distribution of raindrops*. Naturey
603 Physics, 2009. **5**: p. 697-702.
- 604 7. Bartolomé, L. and J. Teuwen, *Prospective challenges in the experimentation of the rain erosion on the*
605 *leading edge of wind turbine blades*. Wind Energy, 2019. **22**: p. 140-151.
- 606 8. Bech, J.I., C.B. Hasager, and C. Bak, *Extending the life of wind turbine blade leading edges by reducing*
607 *the tip speed during extreme precipitation events*. Wind Energy Science, 2018. **3**: p. 729-748.
- 608 9. Eisenberg, D., S. Laustsen, and J. Stege, *Wind turbine blade coating leading edge rain erosion model:*
609 *Development and validation*. Wind Energy, 2018. **21**: p. 942-951.
- 610 10. Slot, H.M., et al., *Leading edge erosion of coated wind turbine blades: Review of coating life models*.
611 Renewable Energy, 2015. **80**: p. 835-848.
- 612 11. Amirzadeh, B., et al., *A computational framework for the analysis of rain-indcued erosion in wind turbine*
613 *blades, part II: Drop impact-indcued stresses and blade coating fatigue life*. Journal of Wind Engineering
614 and Industrial Aerodynamics, 2017. **163**: p. 44-54.
- 615 12. Springer, G.S. and C.I. Yang, *Model for the Rain Erosion of Fiber Reinforced Composites*. AIAA Journal,
616 1975. **13**(7): p. 877-883.
- 617 13. C M Preece, a. and N.H. Macmillan, *Erosion*. Annual Review of Materials Science, 1977. **7**(1): p. 95-121.
- 618 14. Thomas, G.P., J.H. Brunton, and D. Tabor, *Drop impingement erosion of metals*. Proceedings of the Royal
619 Society of London. A. Mathematical and Physical Sciences, 1970. **314**(1519): p. 549-565.
- 620 15. Hu, W., et al., *A computational model of wind turbine blade erosion induced by raindrop impact*. Journal of
621 Physics: Conference Series, 2020. **1452**: p. 012048.
- 622 16. Beard, K.V., V.N. Bringi, and M. Thurai, *A new understanding of raindrop shape*. Atmospheric Research,
623 2010. **97**(4): p. 396-415.
- 624 17. Keegan, M.H., D.H. Nash, and M.M. Stack, *On erosion issues associated with the leading edge of wind*
625 *trubine blades*. Journal of Physics D: Applied Physics, 2013. **46**: p. 383001.
- 626 18. Best, A.C., *The size distribution of raindrops*. Quarterly Journal of the Royal Meteorological Society, 1950.
627 **76**(327): p. 16-36.
- 628 19. McTaggart-Cowan, J.D. and R. List, *Collision and Breakup of Water Drops at Terminal Velocity*. Journal
629 of the Atmospheric Sciences, 1975. **32**(7): p. 1401-1411.
- 630 20. Gunn, R. and G.D. Kinzer, *THE TERMINAL VELOCITY OF FALL FOR WATER DROPLETS IN*
631 *STAGNANT AIR*. Journal of Meteorology, 1949. **6**(4): p. 243-248.

- 632 21. Johnson, R.J., R.A. Stryk, and S.R. Beissel, *SPH for High Velocity Impact Calculations*. Computer
633 Methods in Applied Mechanics and Engineering, 1996. **139**: p. 347-373.
- 634 22. Colagrossi, A. and M. Landrini, *Numerical Simulation of Interfacial Flows by Smoothed Particle*
635 *Hydrodynamics*. Journal of Computational Physics, 2003. **191**(2): p. 448-475.
- 636 23. Gingold, R.A. and J.J. Monaghan, *Smoothed Particle Hydrodynamics: Theory and Application to Non-*
637 *Spherical Stars*. Monthly Notices of the Royal Astronomical Society, 1977. **181**: p. 375-389.
- 638 24. Keegan, M.H., *Wind Turbine Blade Leading Edge Erosion: An Investigation of Rain Droplet and Hailstone*
639 *Impact Induced Damage Mechanisms*. 2014, University Of Strathclyde.
- 640 25. Astrid, B., *Investigation of Droplet Erosion for Offshore Wind Turbine Blades*. Ann. Acad. Med. Stetin.,
641 2014. **59**(1): p. 170-171.
- 642 26. Verma, A.S., et al., *Numerical investigation of rain droplet impact on offshore wind turbine blades under*
643 *different rainfall conditions: A parametric study*. Composite Structures, 2020. **241**.
- 644 27. Stephens, R.I., *Metal Fatigue in Engineering*. 1980, New York: Wiley,1980.
- 645 28. Chen, C., *Fatigue and Fracture*. 2002, Wuhan:Huazhong University of Science and Technology PressS.
- 646 29. C.M. Manjunatha, A.C.T., A.J. Kinloch, S. Sprenger,, *The tensile fatigue behaviour of a silica*
647 *nanoparticle-modified glass fibre reinforced epoxy composite*. Composites Science and Technology,, 2010.
648 **70**(1): p. 193-199.
- 649 30. ASTM, C., *Standard Practices for Cycle Counting in Fatigue Analysis*. 2005: ASTM International, West
650 Conshohocken.
- 651 31. Paris, P., *A Critical Analysis of Crack Propagation Laws* Journal of basic engineering, 1963. **85**(4): p. 528.
- 652 32. Brown, E.N., S.R. White, and N.R. Sottos, *Fatigue crack propagation in microcapsule-toughened epoxy*.
653 Journal of Materials Science, 2006. **41**(19): p. 6266-6273.
- 654 33. Doagou-Rad, S. and L. Mishnaevsky, *Rain erosion of wind turbine blades: computational analysis of*
655 *parameters controlling the surface degradation*. Meccanica, 2019. **55**(4): p. 725-743.
- 656 34. Li, C.-J., et al., *Evolution of Lamellar Interface Cracks During Isothermal Cyclic Test of Plasma-Sprayed*
657 *8YSZ Coating with a Columnar-Structured YSZ Interlayer*. Journal of Thermal Spray Technology, 2013.
658 **22**(8): p. 1374-1382.
- 659 35. Griffith, D.T. and T.D. Ashwill, *The Sandia 100-meter all-glass baseline wnd turbine blade: SNL100-00*.
660 2011, Sandia National Laboratories, Albuquerque, New Mexico, USA.
- 661 36. Mandell, J.F. and D.D. Samborsky, SNL/MSU/DOE composite material fatigue database mechanical
662 properties of composite materials for wind turbine blades version 23.0. Montana State University,
663 Bozeman, 2014.
- 664 37. Gurit. *Structural Core Materials - Gurit Corecell M The Marine Foam (Access on June 21, 2019)*.
665 Available from: [https://www.gurit.com/Our-Business/Composite-Materials/Structural-Core-](https://www.gurit.com/Our-Business/Composite-Materials/Structural-Core-Materials/Gurit-Corecell-M)
666 [Materials/Gurit-Corecell-M](https://www.gurit.com/Our-Business/Composite-Materials/Structural-Core-Materials/Gurit-Corecell-M).
- 667 38. Jones, D.M.A. and A.L. Sims, *Climatology of Instantaneous Rainfall Rates*. Journal of Applied
668 Meteorology, 1978. **17**(8): p. 1135-1140.
- 669 39. Zhou, Q., et al., *Analysis of water drop erosion on turbine blades based on a nonlinear liquid-solid impact*
670 *model*. International Journal of Impact Engineering, 2009. **36**: p. 1156-1171.
- 671

672

673 **ACKNOWLEDGEMENTS**

674 This work is supported by the National Natural Science Foundation of China (NSFC) [grant
675 number 51905475] and the Fundamental Research Funds for the Central Universities [grant
676 number 2019QNA4006].

677

678 **NOMENCLATURE**

679 a Crack depth

680 a_0 Initial crack depth

681 a_c Critical crack depth

682 b Fatigue strength exponent (FSE)

683 C Exponential parameter describing the fatigue crack growth performance of the material

684 d Raindrop diameter

685 D Fatigue damage

686 $D_{1\text{year}}$ Accumulated fatigue damage of the WTB coating per year

687 D_s Damage accumulated over time t_s .

688 h Hight of the tall-column

689 I Rain intensity in mm h^{-1}

690 K Stress intensity factor

691 K_C Fracture toughness

692	K_{\max}	Maximum stress intensity factor
693	K_{\min}	Minimum stress intensity factor
694	m	Linear parameter describing the fatigue crack growth performance of the material
695	$N(V)$	Number of raindrops in volume V
696	N	The number of stress cycles
697	N_c	Number of allowable cyclic stress till the end of the MLR increasing period
698	N_f	Number of allowable cycles in the S-N method
699	N_t	Applied number of stress cycles in one simulated time t
700	P_I	Probability of the rain intensity I
701	r_0	Equivalent spherical radius
702	R	The ratio of the minimum cyclic stress to the maximum cyclic stress
703	t_A	Total rainfall hours per year at a WT location
704	t_f	Expected fatigue life of the WTB coating
705	$t_{\text{incubation}}$	Fatigue life of the erosion incubation period
706	t_I	Total fatigue life under a rain intensity
707	t_{MLR}	Duration of the MLR increasing period
708	t	Duration of the simulated rain in equivalent crack propagation method
709	t_s	Duration of a simulated rain event
710	T	Duration of the simulated rain event

711	UTS	Ultimate tensile strength
712	v	Impact speed
713	V	Unit volume
714	Y	A dimensionless parameter related to the shape of the crack.
715	α	Axis ratio
716	ΔK	Stress intensity factor range
717	$\Delta\sigma$	Average stress amplitude in equivalent crack propagation method
718	θ	Impact angles
719	λ	Expected number of raindrops per unit volume
720	σ_a	Stress amplitude
721	σ'_a	Corrected stress amplitude
722	σ_f	Fatigue strength coefficient (FSC)
723	σ_m	Mean stress
724	σ_{\max}	Maximum stress under one simulated rainfall time period t
725		

726 **TABLE 1** Material properties of the composite panel used in the FEA model [35]

Material Properties	Material Types	Coating	QQ1	Foam
Longitudinal Young's modulus E_1 (GPa)		3.44	33.1	0.256
Transversal Young's modulus E_2 (GPa)		3.44	17.1	0.256
Poisson's ratio ν_{12}		0.3	0.27	0.33
Shear modulus G_{12} (GPa)		1.38	6.29	0.098
Density ρ (kg/m ³)		1235	1919	200

727

728 **TABLE 2** The fatigue life of the blade panel in the MLR increasing period calculated by the crack
 729 propagation method and the equivalent crack propagation method under large rain intensities (11
 730 $\text{mm h}^{-1} \leq I \leq 20 \text{ mm h}^{-1}$).

Rain intensity I (mm h^{-1})	Fatigue lifetime t_1 (min) by the crack propagation method	Fatigue lifetime t_2 (min) by the equivalent crack propagation method	Relative error $\varepsilon = t_1 - t_2 / t_1$
20	209	203	2.87%
19	372	366	1.61%
18	450	446	0.89%
17	781	776	0.64%
16	874	869	0.57%
15	1831	1823	0.44%
14	2637	2631	0.23%
13	2687	2674	0.48%
12	4541	4538	0.07%
11	8168	8163	0.06%

731

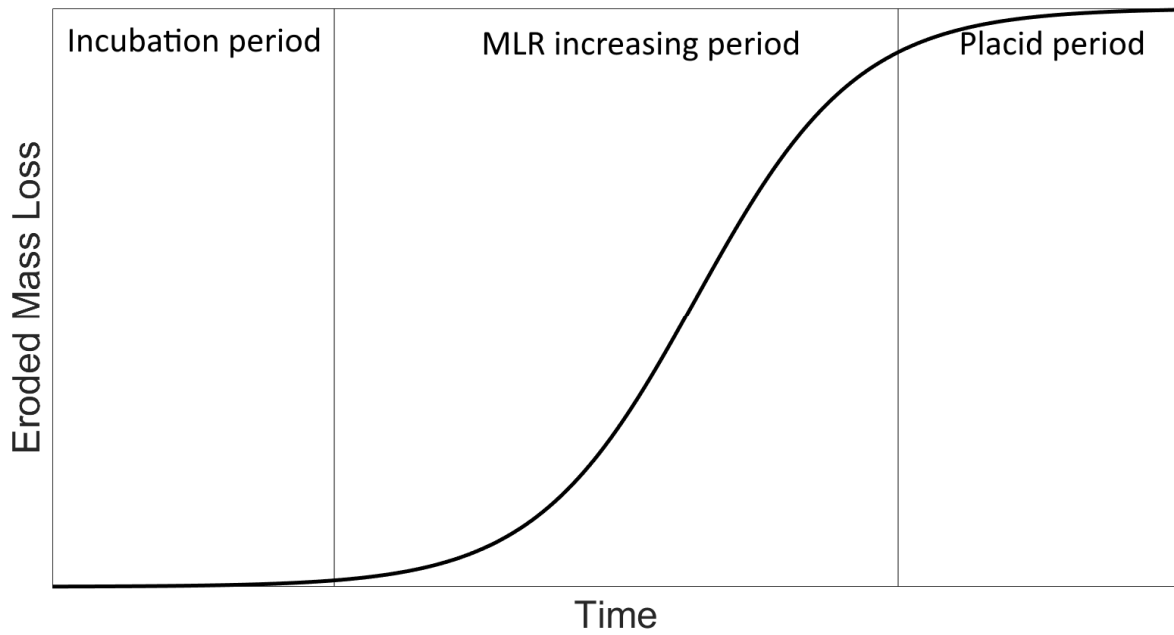
732 **TABLE 3** Coating fatigue life under different rain intensities, impact speeds, impact angles, and
 733 raindrop shapes

Fixed rain parameters	Varied rain parameters	Incubation period (h)	MLR Increasing period (h)	Total Fatigue Life (h)	
Impact Speed=90m/s Impact Angle=90° Raindrop Shape=spherical	Rain Intensity	1 mm/h	10350.00	24966.67	35316.67
		5 mm/h	1.53	12.50	14.03
		10 mm/h	0.52	0.17	0.69
		15 mm/h	0.28	0.10	0.38
		20 mm/h	0.18	0.08	0.26
Rain Intensity=5mm/h Impact Angle=90° Raindrop Shape=spherical	Impact Speed	70 m/s	24.36	357.33	381.69
		80 m/s	2.44	68.63	71.07
		90 m/s	1.53	12.50	14.03
		100 m/s	0.73	1.28	2.01
		110 m/s	0.57	0.15	0.72
Rain Intensity=5mm/h Impact Speed=90m/s Raindrop Shape=spherical	Impact Angle	15°	258.33	1620.00	1878.33
		30°	57.24	610.00	667.24
		45°	15.11	206.17	221.28
		60°	1.77	55.17	56.94
		75°	1.20	10.15	11.35
		90°	1.53	12.50	14.03
Rain Intensity=5mm/h Impact Speed=90m/s Impact Angle=90°	Raindrop Shape	Flat	1.72	37.51	39.23
		Spherical	1.53	12.50	14.03
		Spindle	0.55	0.15	0.7

734 **TABLE 4** Comparison of the total fatigue life in this study and from Bech's result under different
 735 rain intensities

Rain intensity (mm h ⁻¹)	Hours per year (h yr ⁻¹)	Blade tip speed (m s ⁻¹)	Total fatigue life (Bech's result) (h)	Fraction of life spent per year (Bech's result) (%)	Total fatigue life (this study) (h)	Fraction of life spent per year (this study) (%)
20	1.8	90	3.5	51	4.2	42.9
10	8.8	90	79	11	192.7	4.6
5	88	90	3600	2.4	14463	0.6
2	263	90	7.5×10^5	3.5×10^{-2}	1.6×10^6	1.6×10^{-2}
1	438	90	2.8×10^9	1.6×10^{-5}	4.5×10^7	9.7×10^{-4}
Sum of fraction (%):				64.4	X	48.1
Expected life (year):				1.6	X	2.1

736

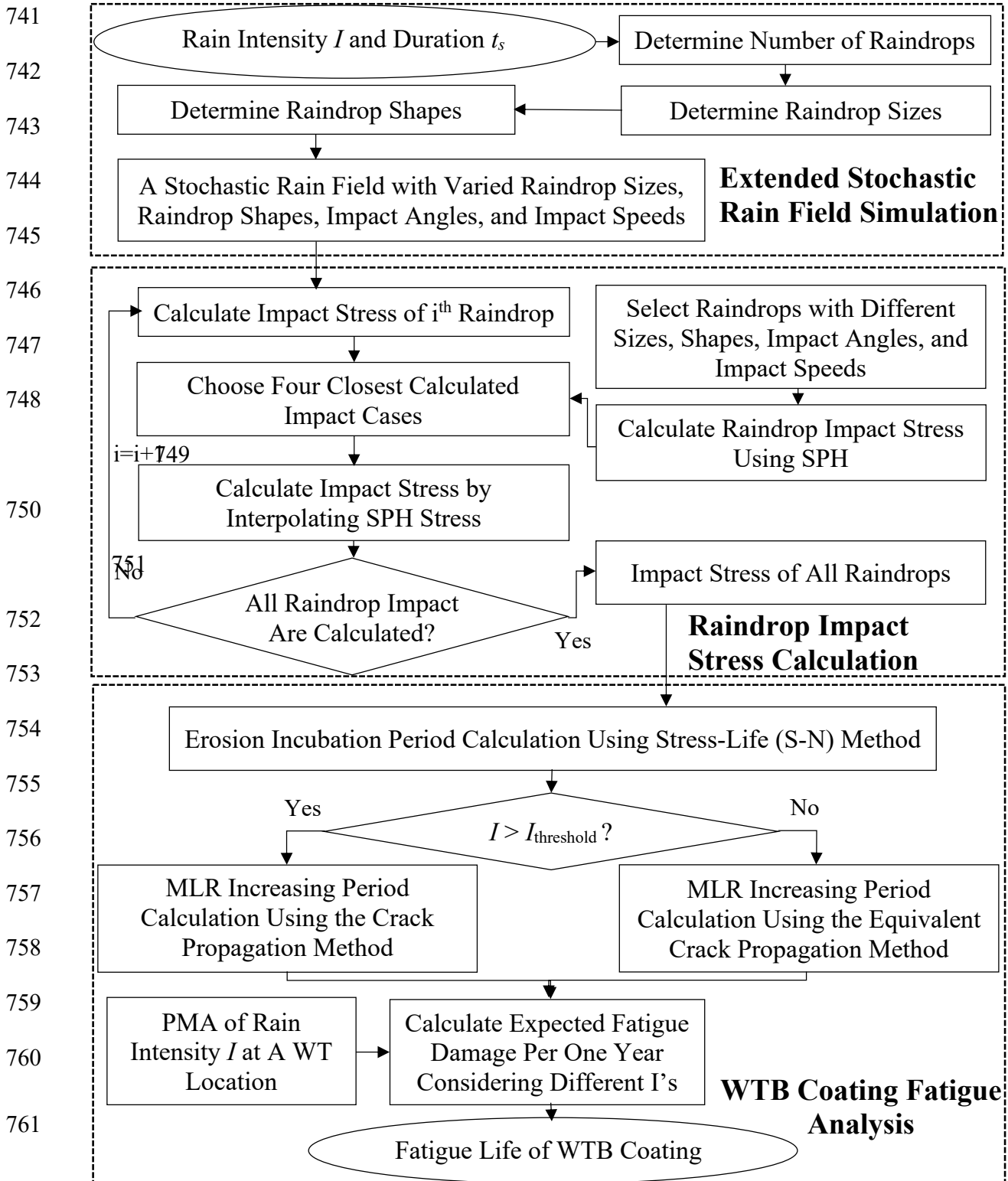


737

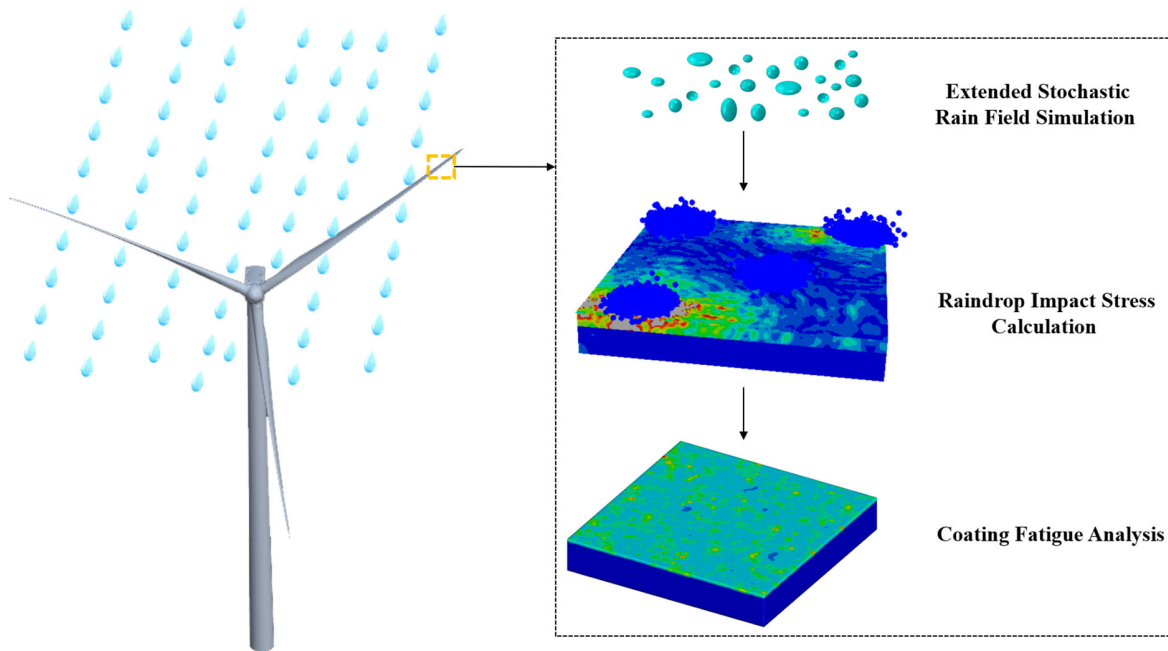
738 **FIGURE 1** Eroded mass loss vs. time in rain erosion. Adapted from Springer and Yang(1975)

739 [12].

740



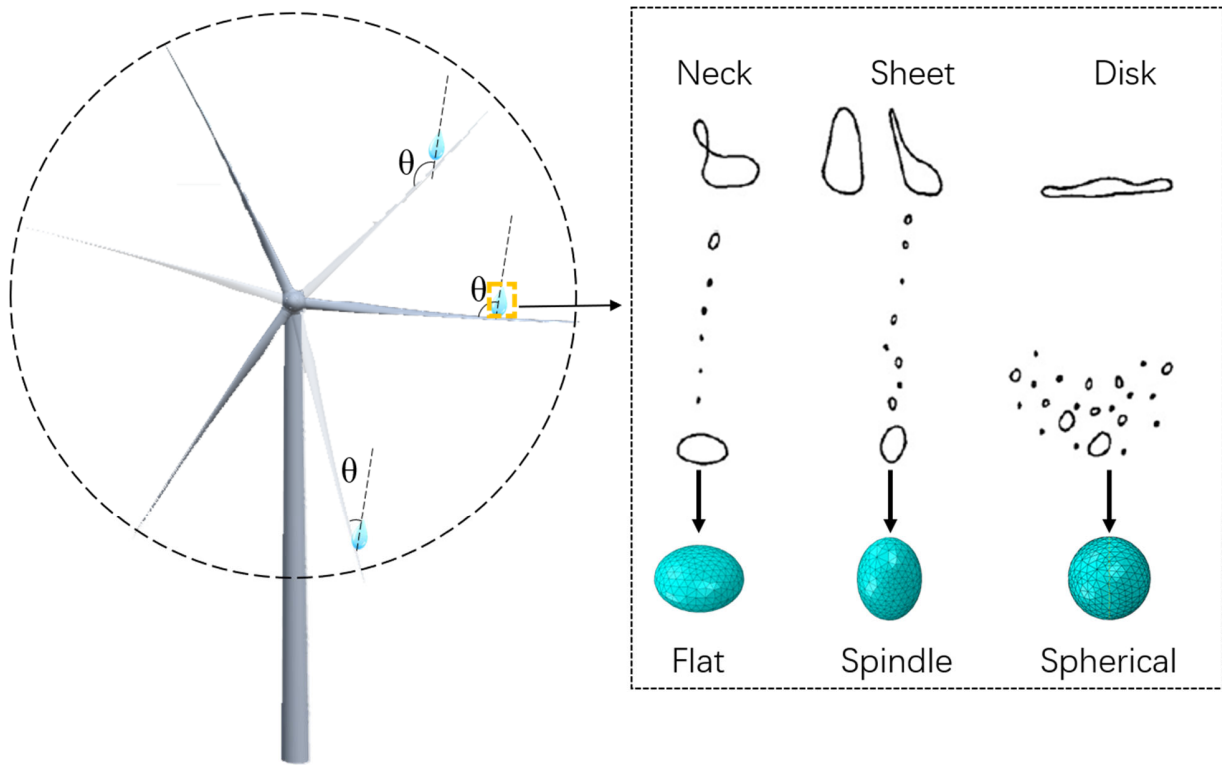
762 **FIGURE 2** The computational framework of wind turbine blade (WTB) coating fatigue due to
763 rain erosion.



764

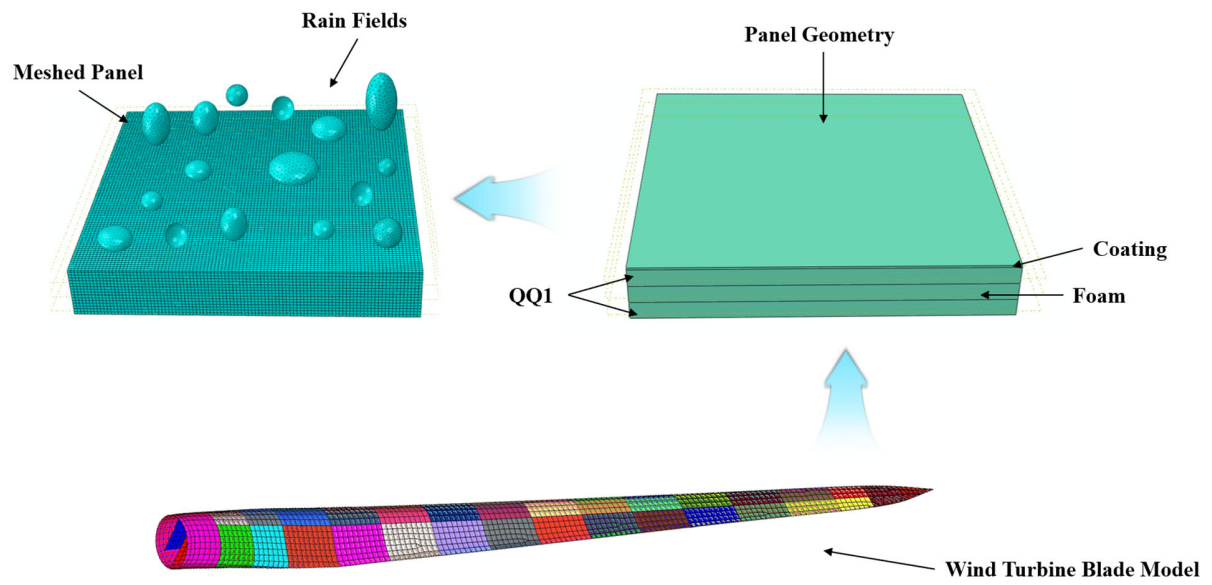
765 **FIGURE 3** Schematic diagram of wind turbine blade coating fatigue induced by raindrop impact.

766



767

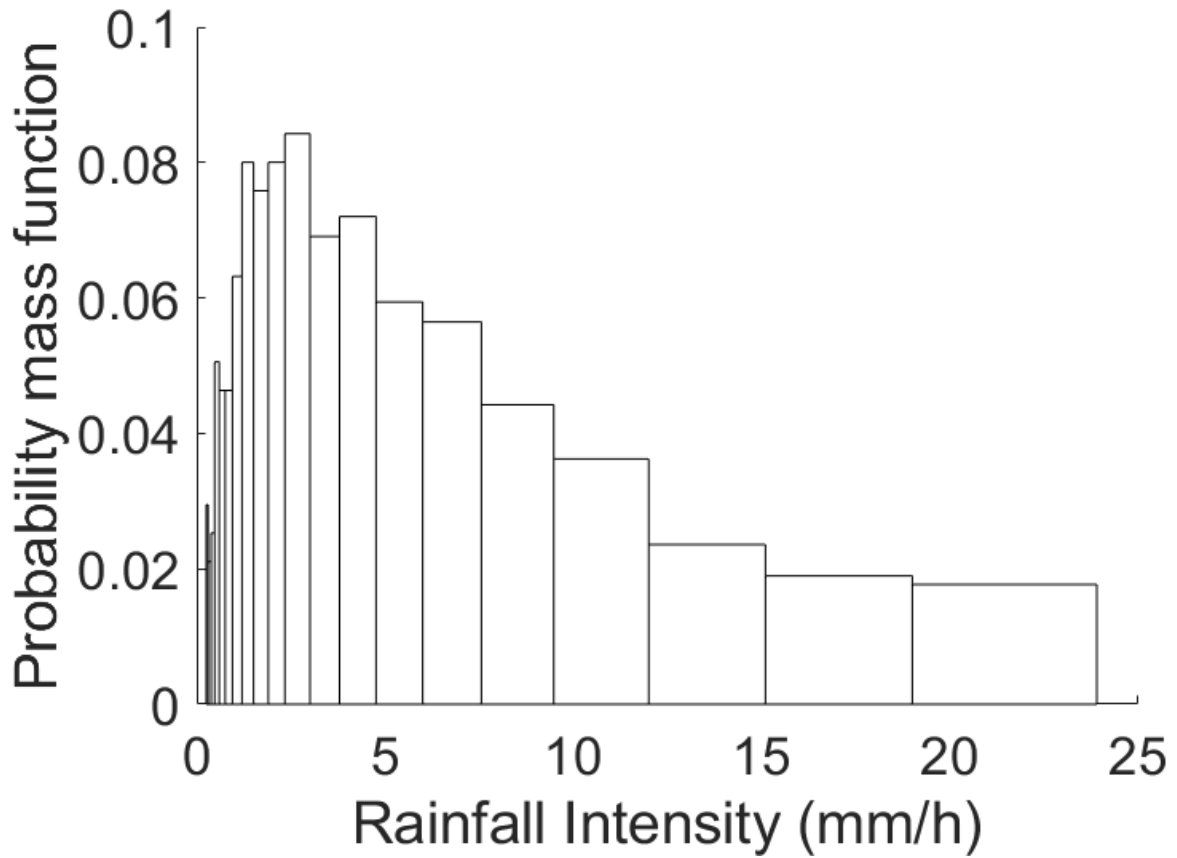
768 **FIGURE 4** Schematic diagram of raindrop shape and impact angle. The flat, spindle, and spherical
769 raindrops correspond to the three predominate breakup types (i.e., neck 27%, sheet 55%, and disk
770 18% from the reference [16]).



771

772 **FIGURE 5** Schematic diagram of raindrops impacting on the panel at the tip of a wind turbine
773 blade.

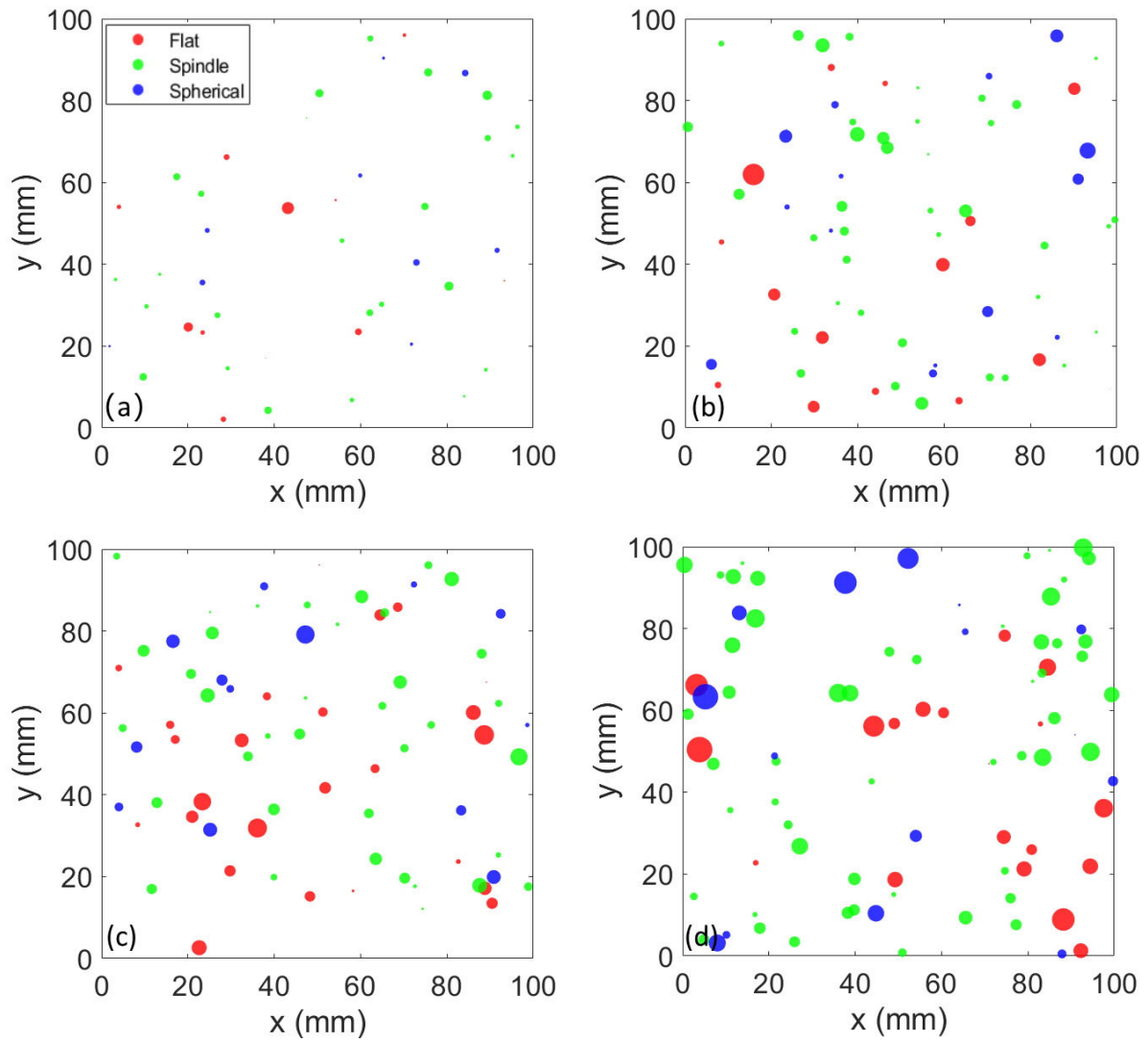
774



775

776 **FIGURE 6** The probability mass function of rain intensity in Miami, FL, from August 1957 to
777 August 1958.

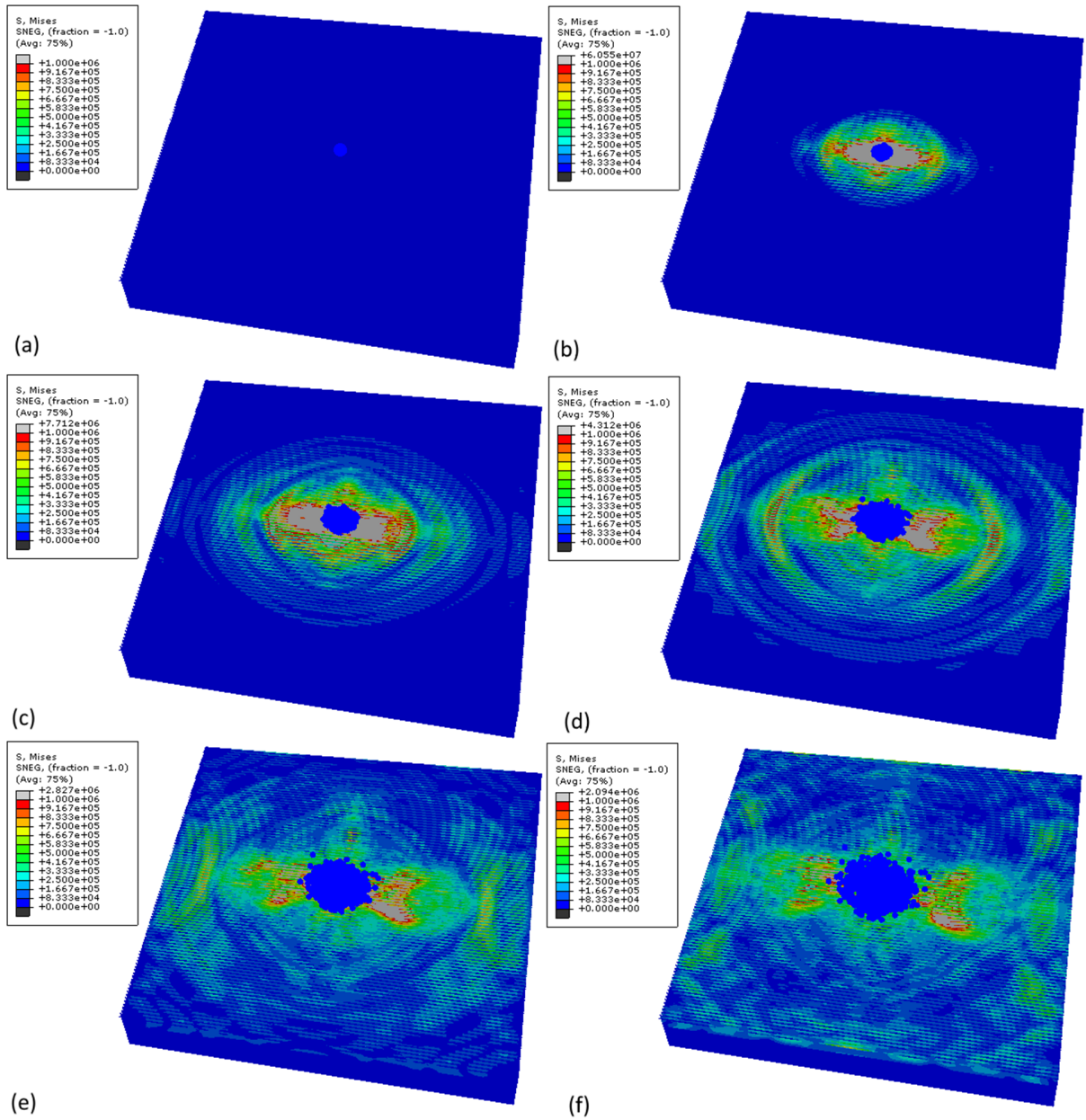
778



779

780 **FIGURE 7** Simulated stochastic rain fields under four rain intensities: (a) 1 mm h^{-1} , (b) 10 mm h^{-1}

781 1 , (c) 20 mm h^{-1} , and (d) 50 mm h^{-1} .



782

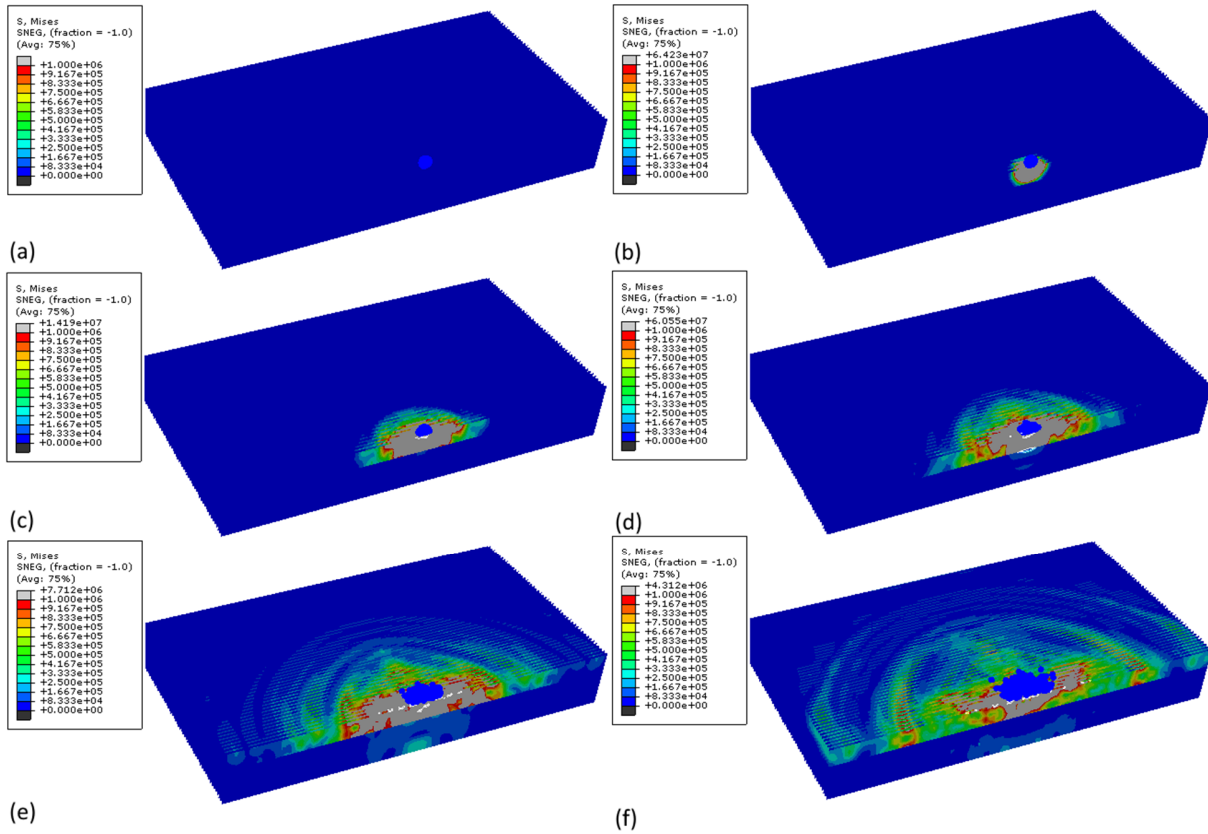
783

784

785

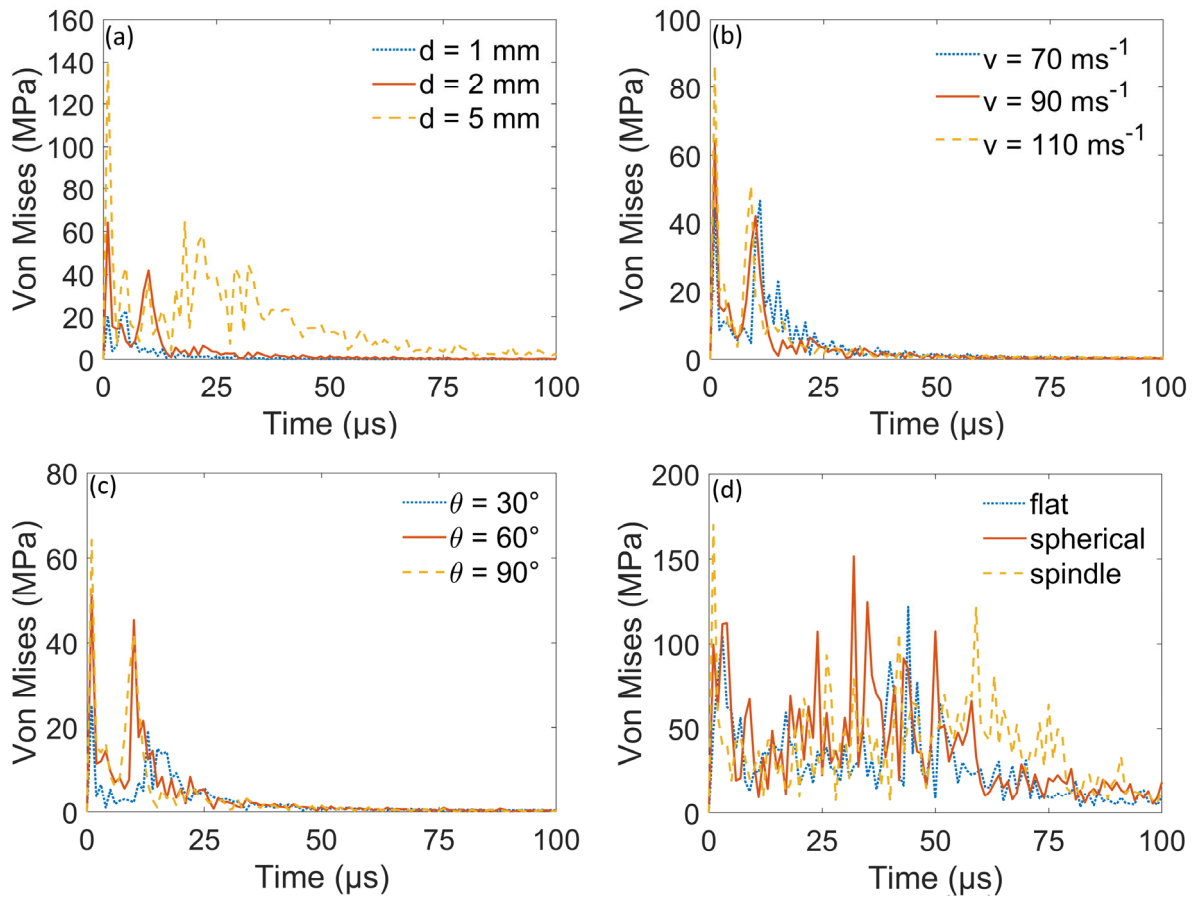
786

FIGURE 8 Simulation of a single raindrop impact. (a-f) von Mises stress contours of the top coating at six time instants ($0 \mu\text{s}$, $10 \mu\text{s}$, $20 \mu\text{s}$, $30 \mu\text{s}$, $40 \mu\text{s}$, $50 \mu\text{s}$) using the raindrop diameter of 2 mm and the impact speed of 90 ms^{-1} .



787 (e) (f)
 788 **FIGURE 9** Simulation of a single raindrop impact. (a-f) cross-sectional views of von Mises stress
 789 contours at six time instants (0 μs , 1 μs , 5 μs , 10 μs , 20 μs , 30 μs) using the raindrop diameter of
 790 2 mm and the impact speed of 90 ms^{-1} .

791

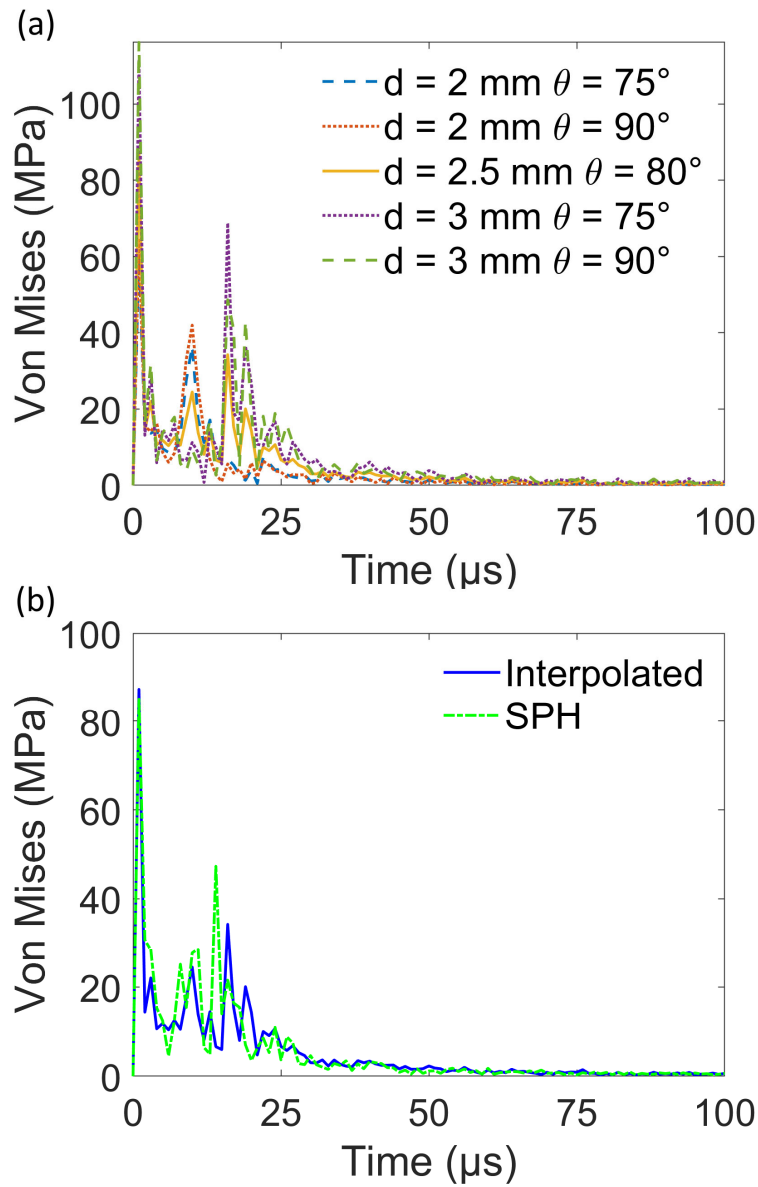


792

793 **FIGURE 10** Comparison of coating von Mises stress considering different (a) raindrop sizes, (b)

794 impact speeds, (c) impact angles, and (d) raindrop shapes.

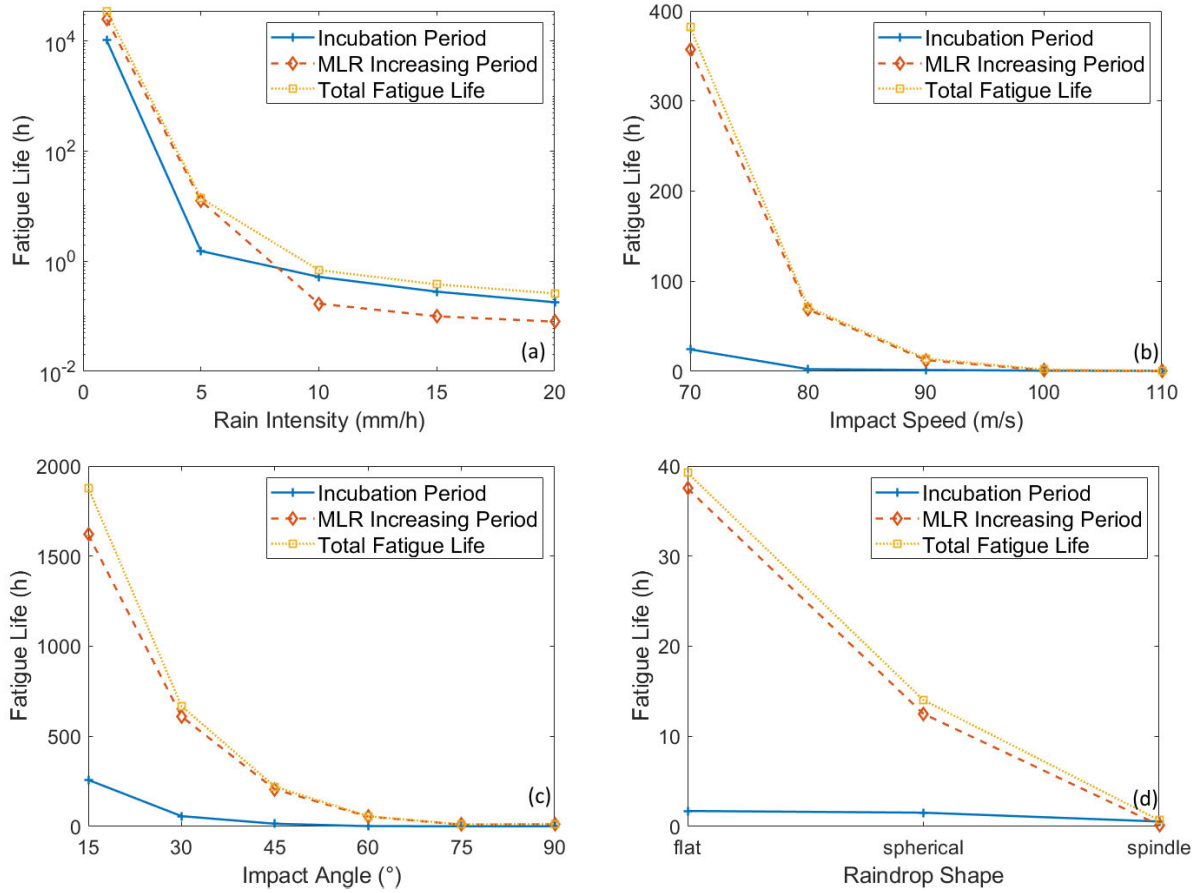
795



796

797 **FIGURE 11** Interpolated impact stress due to a random raindrop (diameter $d = 2.5 \text{ mm}$, spherical
 798 shapes, impact angles $\theta = 80^\circ$, impacting at a top-right corner of the blade panel. (a) Comparison
 799 of the interpolated impact stress and the stresses of the four closet raindrop impact cases; (b)
 800 Comparison of interpolated stress (blue solid curve) and the SPH stress (green dash-dotted curve).

801



802

803 **FIGURE 12** Coating fatigue life corresponding to different (a) rain intensities, (b) impact speeds,

804 (c) impact angles, and (d) raindrop shapes.